Quantum critical dynamics in the two-dimensional transverse Ising model

AUTHOR(S):

Hotta, Chisa; Yoshida, Tempei; Harada, Kenji

PHYSICAL REVIEW RESEARCH **5**, 013186 (2023)

Quantum critical dynamics in the two-dimensional transverse Ising model

Chisa Hotta
Department of Basic Science, University of Tokyo, Komaba, Meguro-ku, Tokyo 153-8902, Japan

Tempei Yoshida
Department of Physics, Kyoto Sangyo University, Kamigamo Motoyama, Kyoto 464-8603, Japan

Kenji Harada
Graduate School of Informatics, Kyoto University, Kyoto 606-8501, Japan

(Received 30 November 2022; accepted 27 February 2023; published 17 March 2023)

In the vicinity of the quantum critical point (QCP), thermodynamic properties diverge toward zero temperature governed by universal exponents. Although this fact is well known, how it is reflected in quantum dynamics has not been addressed. The QCP of the transverse Ising model on a triangular lattice is an ideal platform to test the issue, since it has an experimental realization, the dielectrics being realized in an organic dimer Mott insulator, κ-ET_2X, where a quantum electric dipole represents the Ising degrees of freedom. We track the Glauber-type dynamics of the model by constructing a kinetic protocol based on the quantum Monte Carlo method. The dynamical susceptibility takes the form of the Debye function and shows a significant peak narrowing in approaching a QCP due to the divergence of the relaxation timescale. It explains the anomaly of dielectric constants observed in the organic materials, indicating that the material is very near the ferroelectric QCP. We disclose how the dynamical and other critical exponents develop near QCP beyond the simple field theory.

DOI: 10.1103/PhysRevResearch.5.013186

I. INTRODUCTION

Criticality is a phenomenon characterized by an algebraically growing fluctuation that spreads throughout the system and eventually manifests as a scale invariance of the physical properties [1]. Thermodynamic properties behave critically as the system approaches the second-order phase transition point, which is detected by the divergence of the specific heat and susceptibility. In quantum many-body systems, exponents of such divergence are known to follow the universality that has one extra dimension higher than the space dimension, and this additional dimensional degree of freedom represented by the imaginary time axis is responsible for quantum fluctuation. At low energies or low temperatures, the field theory gives a good description of the states near the quantum critical point (QCP) [2]. The knowledge about static criticality is thus established in both quantum and classical systems, providing reasonable interpretations to the experimental observations in laboratories [3].

However, regarding the dynamics, how the physical properties react to the enhanced quantum fluctuation near the QCP remains unexplored. The difficulty stems primarily from a lack of theoretical tools for evaluating linear response functions in quantum many-body systems [4]. Although it is naively expected that the dynamical exponents will also follow the universality with one extra dimension, quantum relaxation processes remain hard to access even numerically.

In experiments, the dynamical response measurement in an applied field is a very useful technique. Observations at very low temperatures that appear to be influenced by quantum criticality have been reported from time to time, while unfortunately, they cannot be understood within the framework of available theories. One of the intriguing examples is the anomalous dielectric response in a series of triangular lattice Mott insulators, κ-$(ET)_2X$, $X = Cu_2(CN)_3$ [5], and $Cu[N(CN)_2]Cl$ [6]. In these materials, the ET molecules are structurally dimerized and form a triangular lattice in the two-dimensional (2D) conducting layer as shown in Fig. 1(a). Each dimer accommodates a single charge in a Mott insulating phase at low temperature due to strong intradimer electronic correlations [7]. The former material possibly hosts a quantum spin liquid state in the same Mott insulating phase [8]. Deep inside this phase, the temperature-dependent dielectric function shows a peak at $T_m(\omega)$ which shifts significantly to lower temperature as the frequency ω is varied [5]. Although such behavior is reminiscent of relaxer ferroelectrics found typically in PMN [9], the frequency range where the peak shift is observed is much wider, varying over more than two orders of magnitudes. Physically, the peak temperature roughly corresponds to the energy scale dominating the system, and a single divergent peak structure generally suggests a ferroelectric phase transition at that temperature. The observation of frequency-dependent nondivergent peaks indicates a coexisting broad-range distribution of characteristic time and energy

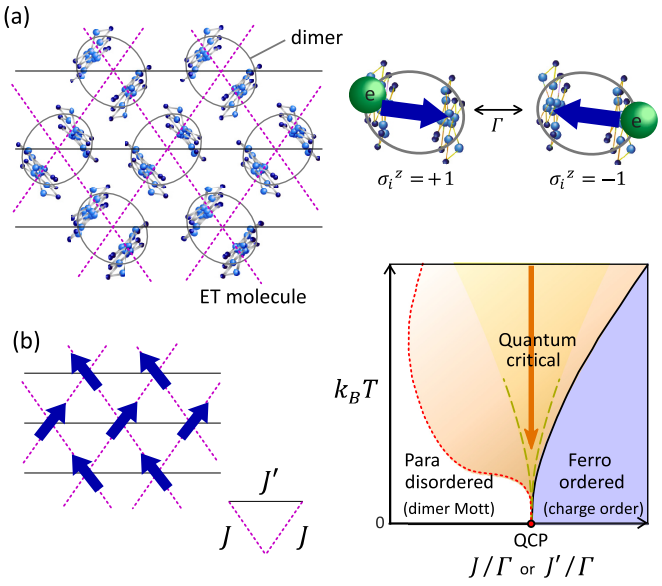

FIG. 1. (a) Two-dimensional conducting plane of κ-$(ET)_2X$. In the insulating phase the electric dipole (right panel) is defined on each dimer as arrows that could point in two different directions depending on the location of the charges. As the charge hops between two molecules, the dipole fluctuates quantum mechanically by Γ. (b) Schematic description of the transverse Ising (TRI) model on an anisotropic triangular lattice. Arrows indicate the Ising degrees of freedom. Phase diagram (right panel) near QCP for the material parameters of κ-$(ET)_2X$ extracted from our results (see Fig. 4). The broken yellow line is the phenomenologically discussed crossover line of the critical region, whereas the region marked with a red dotted line is the one obtained from our calculation where the static and dynamical properties, χ_0 and τ, take enough large values.

scales. In relaxer ferroelectrics, this phenomenon had been attributed to the polar-nano region induced by the artificial impurity doping [9,10]. However, the organic crystals are almost free of impurities.

The Mott dielectrics in organic crystals are attributed to the quantum electric dipole [11]—the degree of freedom of charge to stay at either of the dimerized two molecular orbitals. A good description of this degree of freedom is provided by the transverse Ising (TRI) model [11,12], a canonical model of quantum computation/annealing [13,14] as well as of condensed matter theory. Each charge fluctuates back and forth within the dimer by quantum tunneling via transfer integrals as shown in Fig. 1(a), namely, a transverse electric field is placed on the dipole, and the Coulomb interactions between the charges are the Ising interactions between dipoles. If they align in the same direction, they yield a quantum ferroelectricity [see Fig. 1(b)]. The question is, what could be the reason for the coexisting massive range of energy scales in the dynamics of a disorder-free system at low temperature, and would it be clarified by the microscopic calculation on the TRI model without the aid of simplified phenomenology [15]?

We construct a kinetic protocol based on Glauber dynamics using the quantum Monte Carlo (QMC) method and obtain a dynamic susceptibility, $\chi(q = 0, \omega)$, of the TRI model. We extract the relaxation timescale τ from the Monte Carlo dynamics and show that $\chi(q = 0, \omega)$ turns out to be the Debye function about ω at fixed k_BT whose half-width is given by τ^{-1}. Since both τ and $\chi(q = 0, \omega = 0)$ diverge toward QCP in lowering the temperature, the peak narrowing occurs. This $\chi(q = 0, \omega)$, when viewed as a function of temperature for fixed ω, takes a maximum at $T_m(\omega)$ which significantly decreases with ω due to the peak-narrowing effect. Since $\chi(q = 0, \omega)$ corresponds to the dielectric function of quantum electric dipoles, the aforementioned experimental observation can be understood as the signature of dynamical quantum criticality in the vicinity of the charge ordering transition.

II. MODEL AND FORMULATION

A. Transverse Ising model

Let us introduce the TRI model in a two-dimensional anisotropic triangular lattice:

$$H = \sum_{\langle i,j \rangle} -J_{ij}\sigma_i^z\sigma_j^z - \Gamma \sum_i \sigma_i^x. \tag{1}$$

The z component of the Pauli operator, $\sigma_i^z = \pm 1$, accounts for the location of charges in the ith lattice site representing a dimer, which we call either "pseudospin" or "quantum electric dipole." The transverse field Γ flips the pseudospins up and down via $\sigma_i^x = \sigma_i^+ + \sigma_i^-$, where $\sigma_i^\pm$ represents the raising and lowering operators. We consider the Ising interactions between quantum dipoles J_{ij} on neighboring dimers, i and j. In the anisotropic triangular lattice, we take $J_{ij} = J$ and J' for the bonds along the two directions and the rest, respectively, as shown in Fig. 1(b). We take ferromagnetic $J(> 0)$ while varying J' from antiferromagnetic to ferromagnetic values. This model is obtained by the strong-coupling perturbation theory at the lowest order from the so-called extended Hubbard model [11], a basic model of κ-$(ET)_2X$, which includes the on-site and inter-site Coulomb interaction between electrons and the transfer integrals.

Different configurations of electric dipoles on neighboring dimers have different Coulomb energies, which is the origin of J_{ij} (Appendix A). From the first-principles calculation, the actual parameter values of the extended Hubbard model are precisely evaluated [16–18], and we transform it to our J_{ij} and Γ (see Appendix A). We could thus access the experimentally observed phenomena without bias or assumption by referring to our numerical results with these material parameters.

The dynamical response to the spatially uniform external field $h(t)$, represented by the perturbation $H'(t) = -\sigma_i^z h(t)$ added to Eq. (1), is calculated by the Kubo formula [4]. The susceptibility for wave number q and frequency ω is given as

$$\chi(q, \omega) = \chi(q, 0) + i\omega \int_0^\infty dt e^{i\omega t} \Psi(q, t), \tag{2}$$

which is interpreted in the experiments as a dielectric function, $\epsilon(q, \omega)/\epsilon_0 = 1 + \chi(q, \omega)$ (ϵ_0 is the permittivity of free space), in an applied electric field. Here, $\Psi(q, t)$ is the relaxation function given in an imaginary-time(τ) and real-time(t) connected form as

$$\Psi(q, t) = \int_0^\beta d\tau \langle \sigma_{-q}^z(i\hbar\tau)\sigma_q^z(t)\rangle, \tag{3}$$

where $\sigma_q^z(t) = e^{\frac{iHt}{\hbar}}(\sum_j \sigma_j^z e^{-iqr_j})e^{-\frac{iHt}{\hbar}}$ is the interaction picture of the Ising operator of wave number q. The imaginary time τ that appears as parameter $i\hbar\tau$ in Eq. (3) runs from zero to inverse temperature $\beta = (k_B T)^{-1}$. Since we consider the ferroelectric order of the quantum dipoles, we focus on the case of $q = 0$ in the following.

Conventionally, Eq. (3) is calculated using the finite-temperature Green's function. There one performs the analytic continuation from τ to t, but it is reliable enough only when the analytic form of Green's function is available, which is not the case for strongly correlated quantum systems [2]. Tracking real-time dynamics using numerical time evolution is limited to very small system sizes in the exact diagonalization and to one-dimensional systems by the density matrix renormalization group [19] and matrix product construction [20], which allows for only short timescales. One of the authors developed the nearly exact dynamics of the thermal pure state for a long enough timescale [21], but it is applied so far for $N \lesssim 30$. Recently, the dynamics of the imaginary time evolution is examined in the quantum Monte Carlo study [22,23], which illustrates that the nonadiabatic quantum dynamics at a leading order could be similar to the real-time ones [23]. The generalized dynamical scaling of the susceptibility-like quantity obtained averaged along the imaginary time shows a good collapse [24].

B. Kinetic protocol

Traditional statistical mechanics has provided an idea to implement the dynamics in classical models; it is to consider an isolated system and observe the process of relaxation toward *local equilibrium* during "*the time evolution.*" Glauber dynamics is one such realization using the Markov process [25]; when you apply the Markovian update of the state, a single target spin is locally relaxed quite immediately through the interaction with its surrounding spins that serve as a heat bath. Then "*the time evolution*" using the stochastic process, regardless of whether it is a heat bath method, Metropolis method, or its analogs, was proved to reproduce well the critical behavior, where both static and dynamical exponents are successfully extracted. This was possible because the energetics is determined strictly locally in the classical system with short-range interaction, which does not apply to quantum systems in general.

However, the TRI model exceptionally realizes a quantum local equilibration, to which we can apply the idea of Glauber dynamics. This is because the quantum fluctuation is mediated by the transverse field, which is the on-site fluctuation that has intrinsically the same role as the local thermal fluctuation in that they work to flip the spins locally. Let us first overview the quantum Monte Carlo description of the TRI model. The partition function of the TRI model appears to be the ensemble of world lines running along the imaginary time direction $\tau = [0 : \beta]$ with a periodic boundary, as shown in Fig. 2(a). Since we take the quantization axis parallel to σ_i^z, each point along the ith world line takes either $\sigma_i^z = \pm 1$, and interacts by J_{ij} with the pseudospins on the neighboring jth world line. The quantum fluctuation represented by the transverse field works independently for each site i, and when the pseudospin flips at some imaginary time τ, it is represented by the kink on the world line. The kinks are inserted stochastically following the Poisson distribution and separate the world lines into segments. The weight each segment carries is the integrated classical Boltzmann weight about the Ising interaction with the neighboring pseudospins at the same τ. The Markov process is summarized into the following steps:

1. Choose site i to update,
2. Stochastically generate a series of new kink candidates along the ith world line via the Poisson process with Γ,
3. Separate the world line into segments by old kinks and kinks candidates,
4. Update σ_i^z on each segment $\tau \in [\tau_s : \tau_f]$ following the thermal-bath method using the weight, $\exp[\int_{\tau_s}^{\tau_f} \sum_j J_{ij}\sigma_i^z(\tau)\sigma_j^z(\tau)d\tau]$.
5. We repeat these steps for $i \in [1 : N]$.

The segments are locally updated independently of the rest of the system other than its neighboring segments, which produces the situation of the classical Glauber dynamics. Namely, the above-mentioned Markov process safely relaxes the TRI model toward thermal equilibrium by making use only of the local updates in a unit of segments. Importantly, this process was empirically proved to successfully reproduce the dynamical scaling relation of the TRI model on the square lattice [26]. By taking $\Gamma \to 0$, we find the smooth connection to the Glauber dynamics of the classical Ising model.

We study the dynamical properties using this Markov process which we call a kinetic TRI protocol. The evaluation of Eq. (3) is straightforward. We approximate the two time evolutions to be independent and denote the two variables explicitly as $\sigma^z(\tau, t)$, where the Monte Carlo step, namely, the algorithmic time t, is read off as real time. As in the Glauber dynamics, t is not exactly real time but is regarded as proportional to real time. We measure $\langle\sigma_j^z(\tau, s)\sigma_i^z(0, s+t)\rangle_{\rm eq}$ between σ_i^z of $t = s$ at imaginary time τ and that of $t = s + t$ at imaginary time 0. We take an average over M time steps in the equilibrium as

$$\Psi(r_i - r_j, t) = \int_0^\beta d\tau \langle \sigma_j^z(\tau, 0)\sigma_i^z(0, t)\,\rangle_{\rm eq} \cong \frac{1}{M}\sum_{s=0}^{M}\left\langle\left(\int_0^\beta d\tau\sigma_j^z(\tau, s)\right)\sigma_i^z(0, s+t)\right\rangle, \quad (4)$$

$$\Psi(q, t) = \frac{1}{N}\sum_{i=1}^{N}\sum_{j=1}^{N} e^{-iq(r_i - r_j)}\Psi(r_i - r_j, t). \quad (5)$$

Here the integration over imaginary time τ is made independent of the algorithmic time t. This approximation becomes exact only in the $t \to \infty$ limit. Our QMC calculation is performed for a $N = L \times L$ site cluster with $L = 8, 16, 32, 64, 128$, while taking $L \times k_B T = 8, 4, 1, 0.5$. This is because near the QCP, the minimum temperature that captures the relatively size-free ($L > \xi$) results is limited at each L, and the correlation length ξ diverges in powers. Similarly, the time correlation represented by the relaxation time τ_L extends to more than 10^6 steps near QCP, so that we averaged Eq. (5) over 16 runs, taking $M = 10^7$ time steps for each.

Finally, we notice that some other protocols are applied to quantum annealing [27,28], while they do not fulfill the condition for Glauber dynamics; Ref. [28] includes the loop

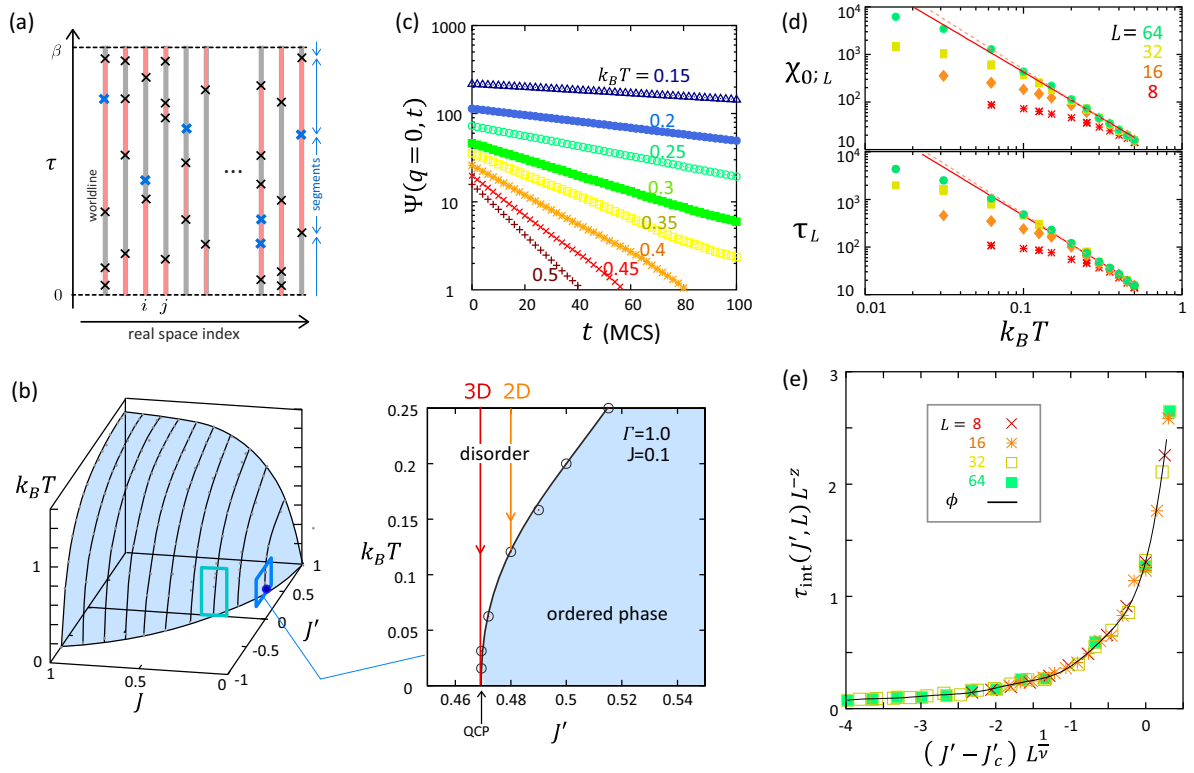

FIG. 2. Results of QMC for the TRI model on an anisotropic triangular lattice given in units of $\Gamma = 1$. (a) Schematic illustration of a set of world lines describing the partition function of the TRI model given on the place of space(i) and imaginary time(τ), which are periodic about $\tau = [0 : \beta]$. Kinks (cross symbols) including old (black) and new (blue) ones separate the world lines into segments and the highlighted/plain segments carry $\sigma^z = 1/-1$. (b) Phase diagram on the plane of J, J', and k_BT. The shaded region corresponds to the ordered phase (ferroelectric order of dipoles). The material parameters of κ-$(ET)_2X$ (Appendix A) fall near the blue point ($J \sim 0.1, J' \sim 0.5$) in the diagram at $k_BT = 0$. The right panel shows the cross section of the phase diagram at $J = 0.1$ at low k_BT in the vicinity of QCP. The case of square lattice ($J' = 0$) in green cross section is given in Appendix C. (c) Relaxation function $\Psi(q = 0, t)$ obtained by the QMC calculation at $L = 64$ and $J' = 0.47, J = 0.1$ for several choices of k_BT. (d) τ_L and $\chi_{0;L}$ extracted from the relaxation function at several L, plotted as functions of k_BT. The envelope lines (broken lines) $\tau = c_1(k_BT)^{-z}$, $\chi_0 = c_2(k_BT)^{-\frac{\gamma}{\nu}}$ are their thermodynamic limit for fitted $z = 2.11$ and $\gamma/\nu = 2.10$. The solid line represents the same function using the 3D critical exponents $z = 2.02$ and $\gamma/\nu = 1.966$ with $c_1 = 4.34$, $c_2 = 4.61$, which is almost the same as the case of square lattice (Appendix C, Fig. 7). (e) Dynamical finite-size scaling analysis. Correlation time $\tau_{\rm int}$ is obtained for a series of $L = 8$, 16, 32, and 64 for $k_BT/\Gamma = 0.5, 0.25, 0.125, 0.0625, 0.031\,25, 0.007\,812\,5$, with $\Gamma/k_BT = 2L$. The data collapse to a single scaling function ϕ.

update, and Ref. [27] performs simultaneous flipping of a variable along the whole imaginary time. Particularly in the latter, the relaxation process may change and shall be discriminated from Ref. [26]. We briefly note that there are some other trials, like a phenomenological extension of the Glauber dynamics to quantum systems [29], or variational Monte Carlo approaches regarding time evolutions [30], and semiclassical approximation using the discrete Monte Carlo sampling in phase space [31].

III. RESULTS

A. Phase diagram

We first overview the low-temperature properties of the TRI model on an anisotropic triangular lattice. Overall, at large enough J_{ij}/Γ, the system is in an ordered phase, while the increase of Γ makes the system disordered, and the phase transition between the two is typically second order. We show the $k_BT - J - J'$ phase diagram in Fig. 2(b) in units of $\Gamma = 1$ obtained by the present QMC calculation. We made a Binder plot of the pseudospin magnetization $m = \sum_j \sigma_j^z/N$ to evaluate the phase boundaries at low temperatures, and the higher temperature T_c's are evaluated by the specific heat data (see Appendix B and Fig. 6 for details).

The ordered phase extends from the large $J, J' > 0$ region toward slightly antiferromagnetic J'. The case of the square lattice ($J' = 0$) is well studied [26,32], and the phase boundary at $k_BT = 0$ (QCP) is evaluated as $J_c/\Gamma = 0.3284(9)$ [26]. From a series of first-principles calculations, a family of κ-$(ET)_2X$ is located at around $J \sim 0.1, J' \sim 0.5$ (Appendix A) [16], which is marked in Fig. 2(b). One finds that it is near the QCP.

B. Relaxation function

In the disordered phase relatively near the phase boundary, the relaxation function $\Psi(q = 0, t)$ shows a clear exponential decay as a function of a QMC time step typically as in

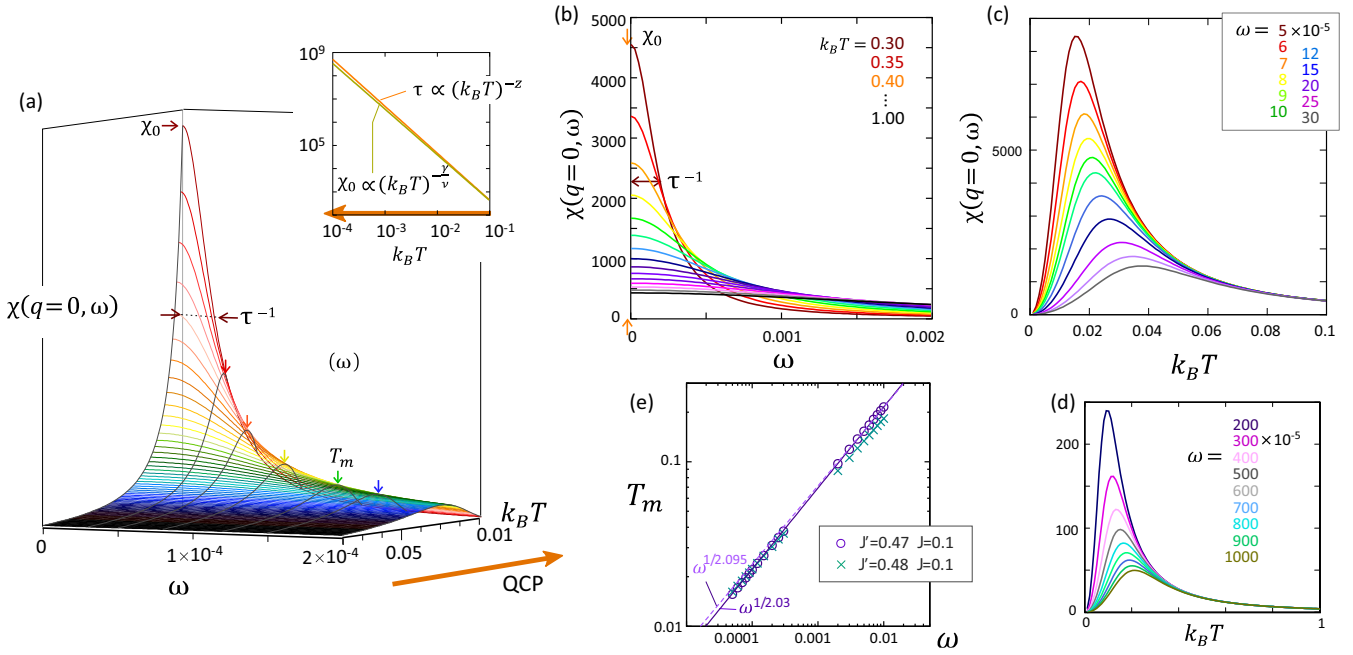

FIG. 3. Dynamical susceptibility $\chi(q=0,\omega)$ obtained by the kinetic TRI protocol as functions of ω and k_BT. (a) Three-dimensional plot showing a set of Debye functions about ω for different choices of k_BT. We choose $(J',J)=(0.47,0.1)$ that exhibits QCP in Fig. 2(b). Inset shows the temperature dependence of τ and χ_0 used for this plot and are extracted from the relaxation function. Small arrows indicate the peak positions, $T_m(\omega)$. (b) ω dependence of $\chi(q=0,\omega)$ for several choices of k_BT. The half-width of the $q=0$ peak gives τ^{-1} and its peak height gives χ_0. (c, d) Temperature dependence of $\chi(q=0,\omega)$ for several choices of ω, ranging over $5-30\times10^{-5}$ and $2-10\times10^{-3}$. (e) ω dependence of T_m for the QCP data [in panels (c, d)] and for slightly off QCP, $(J',J)=(0.48,0.1)$. Solid and broken lines are $\propto\omega^{1/2.03}$ fitted by the QCP data and $\omega^{1/z}$, $z=2.095$, respectively.

Fig. 2(c), which can be described as

$$\Psi(q=0,t)=\chi_{0;L}\exp(-t/\tau_L), \tag{6}$$

using the static uniform susceptibility, $\chi_{0;L}$, and the relaxation time τ_L at fixed k_BT, J, J', and L. The extracted values of $\chi_{0;L}$ and τ_L are plotted in Fig. 2(d) for $L=8$, 16, 32, and 64 as functions of k_BT at $J'=J'_c$. Data points belonging to different L follow different curvatures, which converge to an envelope function: they are the values at the thermodynamic limit, given as $\tau\propto(k_BT)^{-z}$ and $\chi_0\propto(k_BT)^{-\gamma/\nu}$. When the correlation length ξ exceeds L at low k_BT, the data points fall off from the envelope function. Here we plot the case of $z=2.02$ and $\gamma/\nu=1.966$ as a solid line for the three-dimensional (3D) universality class at the QCP, while the broken lines obtained by leaving z and γ/ν as fitting parameters are shown as a reference.

C. Finite-size scaling analysis

We now test the similarities between the present kinetic TRI protocol and the original TRI model by the generalized dynamical finite-size scaling analysis; the scale invariance is expected in the dynamical critical phenomena, which results in the finite-size scaling form of the relaxation timescale near QCP, given as

$$\tau_{\rm int}(J',L)=L^z\phi[(J'-J'_c)L^{\frac{1}{\nu}}], \tag{7}$$

where z is the dynamical critical exponent, and ν is the critical exponent characterizing $\xi\propto|J'-J'_c|^{-\nu}$. We evaluate $\tau_{\rm int}$ at low temperatures available in a series of $k_BT=\Gamma/2L$ down to $k_BT=0.007\,812\,5\Gamma$ with $\Gamma=1$ by varying J' in the phase diagram of Fig. 2(b). We use the following integral:

$$\tau_{\rm int}=\int_0^\infty\Psi(q=0,t)\Big/\Psi(q=0,0)dt, \tag{8}$$

which gives the value independent of the detailed functional form of $\Psi(q=0,t)$. Figure 2(e) shows the finite-size scaling plot using $L=8$, 16, 32, and 64. One finds an almost perfect collapse of the data points into a single functional form. The exponent obtained by this plot is $J_c/\Gamma=0.4700$, $(z,1/\nu)=[2.095,1.56(3)]$, which is fully consistent with our Binder analysis of TRI and the fitting of exponents on the kinetic TRI. We thus think it to be properly interpreted as a 3D universality class.

D. Susceptibility and critical exponents

We have shown that the relaxation function decreases exponentially with t as Eq. (6), and one can extract from a series of $\chi_{0;L}$ and τ_L, their $L\to\infty$ limit, τ and χ_0. Since the system is near QCP, τ and χ_0 diverge in powers toward the ordered phase as [see the inset of Fig. 3(a)],

$$\tau(k_BT)=c_1(k_BT)^{-z},\quad \chi_0(k_BT)=c_2(k_BT)^{-\frac{\gamma}{\nu}}, \tag{9}$$

where γ is the magnetic critical exponent and c_i are the constant coefficients. This could be understood as follows: Consider a quantum 2D system of size $L\times L$ with an additional axis in the imaginary time direction $[0:\beta]$ that

characterizes quantum fluctuation. As the system approaches QCP, the correlation length ξ diverges. Suppose that L is large enough to assume $L > \xi$, and then β becomes the upper bound of the effective system length. For moderately low temperatures, ξ cannot develop larger than β. From the scaling theory we immediately find $\tau \propto \xi^z = (k_B T)^{-z}$. The form Eq. (9) is applied to laboratory systems as well as to theoretical models.

The criticality at QCP and off QCP in the ordered region follows that of the 3D and 2D (kinetic) Ising universality classes [1,2] [the two lines in the right panel of Fig. 2(b)], and their exponents are evaluated as $(z, \gamma, \nu) = (2.02$ [33],–2.03 [34], 1.237, 0.629 [35],–0.630 [36]) and (2.165 [37],–2.18 [38,39], 1.75,1), respectively. We analyzed the QMC data precisely and found good agreement with these exponents (Appendices C and D, Fig. 7). The envelope of Fig. 2(d) follows these exponents. It is notable that c_1 and c_2 do not seem to depend on the location of QCP in the phase diagram.

The dynamical susceptibility in Eq. (2) is a Fourier transform of Eq. (6), which is given analytically in the Lorentzian form as

$$\chi(q = 0, \omega) = \chi_0 \frac{\tau^{-2}}{\omega^2 + \tau^{-2}}. \tag{10}$$

It corresponds to the Debye function in dielectrics. The cross sections of Fig. 3(a) at fixed values of $k_B T$ and ω are shown in Figs. 3(b) and 3(c), respectively. The frequency dependence of $T_m(\omega)$ near QCP is scalable, namely, if we take the temperature range one order of magnitude higher than that of the main panel of Fig. 3(c), almost the same functional form is observed by shifting the frequency to the higher energy [Fig. 3(d)].

Let us apply the scaling analysis to the dynamical susceptibility. Remembering the form of χ_0 in Eq. (9) at $|J' - J'_c| \to 0$, one can express Eq. (10) as $\chi(T, \omega) = T^{-\gamma/\nu} \psi(\omega\tau)$. In finite-size systems, in approaching QCP the correlation length cannot exceed $\xi \sim \beta$ and accordingly, $\tau \propto \xi^z \sim T^{-z}$, which means that $\chi(T, \omega) = T^{-\gamma/\nu} \psi(\omega T^{-z})$. The peak position of this function fulfills

$$T_m \propto \omega^{1/z}. \tag{11}$$

The data points shown in Fig. 3(e) obtained from Figs. 3(c) and 3(d) indeed follow this power law dominated by the dynamical critical exponent. As we discuss shortly, this behavior is in good agreement with the dielectric experiments on κ-$ET_2Cu_2(CN)_3$.

By precisely evaluating the data by the QMC calculation and from the size scaling, we obtain a set of (χ_0, τ) in Eq. (10) over the whole region of the phase diagram. Their contour maps are given in Fig. 4. In the region $\tau < 10$ we are no longer able to perform the fitting of Eq. (6), which is marked as a red broken line in Fig. 1(b). The corresponding behavior for the case of the square lattice ($J' = 0$) is shown in Appendix C, Fig. 7. In Fig. 1(b) we wrote two broken lines that develop from QCP, generally expected as a naive and schematic description of the crossover line from the critical to the disordered region. However, our calculations show that in reality, there is no discipline to determine such crossover. Indeed, such behavior is only applied at extremely low $k_B T \lesssim 0.05$, above which the contour lines show model-dependent shapes that follow the phase boundary. Our calculations show

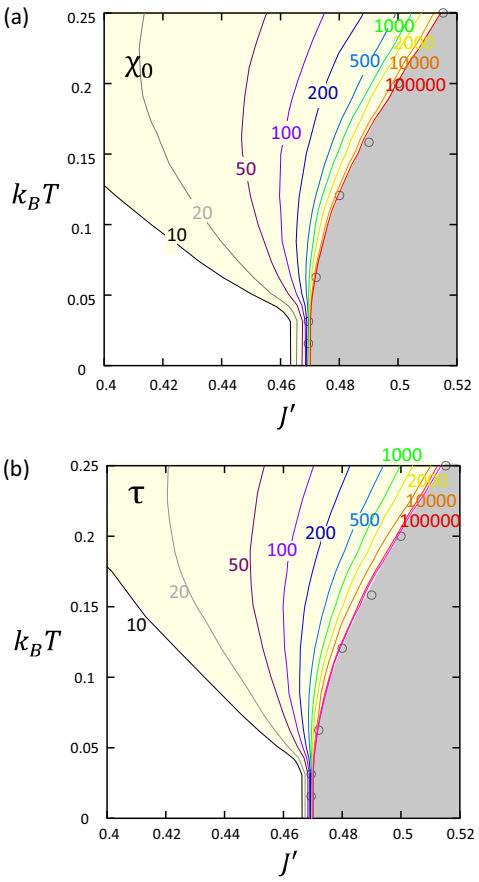

FIG. 4. Density map of (a) static susceptibility χ_0 and (b) the relaxation time τ extracted from the envelope of the relaxation function, plotted as functions of $k_B T$ for the TRI model on a triangular lattice taking $\Gamma = 1$ as a unit.

that the criticality that follows that conventional picture is observed at a much lower temperature than usually expected.

IV. SUMMARY AND DISCUSSION

We have clarified how quantum criticality appears in the dynamics of the quantum many-body system. As an ideal and realistic platform, we chose the TRI model on an anisotropic triangular lattice, whose Ising degrees of freedom represent the quantum electric dipole degrees of freedom in the dimer Mott insulating phase of the organic crystal, κ-ET_2X. The same set of calculations is also performed for the case of the regular square lattice to confirm that the results are not dependent on the model parameters. The model is known to exhibit a quantum criticality and can be almost exactly solved numerically by the quantum Monte Carlo method. We developed a kinetic TRI protocol to study the quantum dynamics of the TRI model, which is built on the local quantum Monte Carlo update of segments of world lines running in the imaginary time directions. This Markov update enables a rapid local equilibration of each segment that can be mapped to the case of classical Monte Carlo updates of higher dimensions. Since the latter is known to capture the intrinsic real-time Glauber-type dynamics, our Monte Carlo time can mimic real-time relaxation in the same context, allowing us

to study the semiclassical dynamics representing the quantum dynamics of the original model.

In this protocol we obtained the dynamical susceptibility by analyzing the Monte Carlo time dependence of the correlation functions and showed that they have Debye functional form with its peak heights and inverse of width diverging algebraically in approaching QCP. This led to a significant peak narrowing, and the obtained temperature dependence of the dynamical susceptibility is found to show a frequency-dependent peak shift reminiscent of the relaxor-ferroelectric-like behavior observed in many experimental studies of organic dimer Mott materials [40,41].

We briefly refer to some theoretical studies discussing this relaxor-ferroelectric-like behavior of κ-ET_2X. The extended Hubbard model in one dimension is studied at the mean-field level using the phase Hamiltonian [15], which they aim to represent phenomenologically using the cross-section line of the 2D systems. They discussed the kinks (the domains in 2D) as the origin of frequency-dependent peaks, and by evaluating the dynamical correlation function of kinks, showed that their relaxation timescale shall vary with frequency by orders of magnitudes. This may give one simplified interpretation of part of the phenomena; however, they do not explain a temperature-dependent characteristic dynamical susceptibility, and the phenomena seem to have no relevance to the criticality we observed.

The authors in Ref. [42] have studied the analog of the effective model in Ref. [11] for κ-ET_2X. They discarded the quantum fluctuation term and performed the classical Monte Carlo study, where they took account of the electron spin as a classical SO(3) vector which coupled with the electric dipole described as Ising pseudospins, showing that the two will generate a dynamical (classical) disorder to each other. The dipole susceptibility shows broad peaks in lowering the temperatures, which they attributed to the glassiness; it may be relevant to the glassy behavior of κ-$ET_2Cu_2(CN)_3$ at $T < 6$ K [5]. Indeed, the coupling of two different degrees of freedom can be a driving force of glassiness. Recently, one of the authors and collaborators showed that in a three-dimensional frustrated pyrochlore lattice, the model including the spin and lattice-displacement coupling can exhibit a thermodynamic glass transition at finite temperature even without quenched disorder [43], which explained the long-standing puzzle on the origin of the disorder-free spin glass in $Y_2Mo_2O_7$ [44]. Since the classical model in Ref. [42] is 2D, the fluctuation disturbs the true glass transition and the system remains glassy. If one deals with it quantum mechanically, there shall be room for the true glass transition [45].

We now compare the overall behavior of $\chi(q = 0, \omega)$ with the experimentally observed [5,6] dielectric constant $\epsilon'(\omega)$ of κ-$(ET)_2X$. The material at ambient temperature is a good conductor. At temperatures below 100 K, the charges start to lose their conductance and localize on each dimer, and a quantum electric dipole is spontaneously formed due to strong electronic correlations [11]. This electric dipole emerges due to the special modulation of wave function (charge distribution), which should be discriminated from the conventional and semiclassical lattice-displacement types of dielectrics [46]. As the frequency is varied from 1 to 100 kHz, the peak position of the dielectric constant of κ-$(ET)_2Cu_2(CN)_3$ shifts from about 20 to 50 K. By extracting $\epsilon'(\omega)$ within this temperature window and fitting them by Eq. (10), we find a series of Debye curves belonging to different T that crosses in a manner comparable to Fig. 3(b) (Appendix E). In the case of κ-$(ET)_2Cu[N(CN)_2]Cl$, only slight variation of $T_m(\omega) \sim$ 25–30 K is found, with no such crossings, and is considered to locate off the QCP.

One remaining issue is that we cannot directly determine the laboratory timescale that corresponds to the Monte Carlo time step. Still, we may safely assume that for each temperature $t = a(T)t_{\rm lab}$ holds, where $a(T)$ could become smaller with lowering the temperature by a few factors. If we plot the extracted value of τ for κ-$(ET)_2Cu_2(CN)_3$ against $(T - T_c)$, taking $T_c = 6$ K where the Curie tail of $\epsilon'(\omega)$ diverges [5], we obtain $\tau_{\rm lab} \propto (T - T_c)^{z_{\rm lab}\nu}$ with $z_{\rm lab}\nu \sim$ 2–3 (Appendix Fig. 9) not too different from that of the 2D Ising ones expected for the parameter region having nonzero T_c.

Although there had been a dispute on whether such seemingly subtle dipole really exists [47,48], further examination of κ-$(ET)_2Cu[N(CN)_2]Cl$ after Ref. [6] for many samples supported the picture of the order-disorder type of ferroelectrics [49]. The dipoles have further proven to be present in β-$(ET)_2ICl_2$, a similar 2D material showing the same critical dynamics, via observation of pyrocurrent [50], collective mode [51], and the polarization curve [52]. The noise measurements on β-$(ET)_2ICl_2$ suggest an emergent nanoscale polarized cluster [41] which is apparently not due to impurities. The phenomenon is not restricted to ET systems, as it is observed in another dimer Mott insulator, β'-type $Pd(dmit)_2$ [40]. Similar dynamics is quite relevant near the phase transition in a series of quasi-one-dimensional organic materials $TMTSF_2X$ [53,54] based on dimerized molecules, although its criticality was not really discussed before.

The quantum nature of dielectrics has become a topic in a series of materials. A geometrical frustration-induced quantum paraelectric nature is found in the conventional displacement-type of dipoles in a hexaferrite $BaFe_{12}O_{19}$ [55]. Critical behavior of the static dielectric function has been discussed in another displacement-type of quantum paraelectric, $SrTiO_3$, on the basis of a phenomenological ϕ^4 theory, which explains well the experimental observation in such a 3D system with quantum fluctuation [56]. Then finally, the present study reached the dynamics of dipoles in the presence of strong quantum fluctuation characteristics of two dimensions. The TRI model adopted here may serve as an intersection of material science in laboratories and the modern theories of computational science.

ACKNOWLEDGMENTS

This work was supported by a Grant-in-Aid for Transformative Research Areas, "The Natural Laws of Extreme Universe, A New Paradigm for Spacetime and Matter from Quantum Information" (Grant No. 21H05191) and by JSPS KAKENHI (Grants No. 21K03440 and No. 18H01173) of Japan. We thank the experimentalists, Takahiko Sasaki, Ichiro Terasaki, Jens Mueller, Peter Lunkenheimer, Michel Lang,

and Martin Dressel, for fruitful communications. We also thank Sei Suzuki for the discussions.

APPENDIX A: MICROSCOPIC DERIVATION OF THE MODEL PARAMETERS

We evaluate the model parameters of κ-ET$_2X$ based on the first-principles calculation reported by one of the authors [16]. Figure 5 shows the schematic description of the 2D conducting layer of κ-ET$_2X$, where the circle represents an ET molecular orbital (which we call here "sites") and the oval a dimer. There are four sites and two dimers in the unit cell. This family of material has an old history [7], and is well described by the extended Hubbard model in a unit of molecular orbitals as [57]

$$\mathcal{H} = \sum_{\langle i,j\rangle}\sum_{\sigma=\uparrow,\downarrow} -t_{ij}(c^\dagger_{i\sigma}c_{j\sigma} + \text{H.c.}) + \sum_{i=1}^{N} U n_{i\uparrow}n_{i\downarrow} + \sum_{\langle i,j\rangle} V_{ij} n_i n_j, \tag{A1}$$

where $c^\dagger_{i\sigma}/c_{i\sigma}$ is the creation/annihilation operator of electrons on site i and spin σ, and $n_{i\sigma} = c^\dagger_{i\sigma}c_{i\sigma}$, $n_i = n_{i\uparrow} + n_{i\downarrow}$ are their number operators. The transfer integrals t_{ij} are evaluated from the latest first-principles calculation as (Tables I and II of Ref. [16]), $(t_2, t_3, t_4) = (0.46, 0.43, -0.08)$ and $(0.34, 0.51, -0.21)$ for $X = \text{Cu}_2(\text{CN})_3$ and Cu[N(CN)$_2$]Cl, respectively, in units of t_1, showing that the geometry of t's depends on materials. The intradimer transfer integral is not much different between materials: $t_1 = 199$ meV and 207 meV for $X = \text{Cu}_2(\text{CN})_3$ and Cu[N(CN)$_2$]Cl, respectively. They take 195–209 meV for all other κ-ET$_2X$ studied in Ref. [16]. The on-site Coulomb U and the inter-site Coulomb interactions V_{ij} are also evaluated based on the molecular distances (x-ray structure) [16] referring to the *ab initio* down-folding [17], which are $U = 8$, $(V_1, V_2, V_3, V_4) = (4.0, 2.0, 2.4, 2.0)$ in units of $t_1 = 200$ meV (or $V_2 \sim 0.4$ eV), also almost independent of X. While the amplitudes of these interactions are overestimated, the ratio between these interactions shall be safely adopted.

Let us consider the strong-coupling case, $U, V_1 \gg V_i, t_i$, where the electrons do not occupy the same site nor the dimer. There are $4^2 = 16$ basis states in a dimer, but this is reduced to 4 in the strong-coupling case [see Fig. 5(b)]. One of the authors has derived the effective Hamiltonian by the perturbation up to the fourth order [11], where the second-order perturbation is responsible for the coupling of the spin and charge degrees of freedom, whereas the leading order (namely, first order in t_{ij}) does not include the spin operator, as the spins can only hop within dimers. Therefore taking only the lowest order reduces the number of basis per dimer to 2, in which the configuration of charge degrees of freedom in the dimer is represented via the up and down of pseudospins, $\sigma^z_i = \pm 1/2$. The effective Hamiltonian is reduced to the representation of $m = 1 \sim 2^N$ basis,

$$\mathcal{H}^{(1)}_{\text{eff}} = \sum_{m,m'} \langle m|H_{mm'}|m'\rangle = \sum_i -J_{ij}\sigma^z_i\sigma^z_j + \Gamma\sum_{i=1}^{N}\sigma^z_i, \tag{A2}$$

where $\Gamma = t_1$ and $J = (V_3 - V_4)/4$, $J' = V_2/4$. The intradimer transfer integral moves the charge back and forth, which works as a transverse field that flips the pseudospins. Regarding the interdimer interaction, the energy difference between the two different classical configurations of pseudospins amounts to $2J_{ij}$, which are given by that of the original Hamiltonian as the difference of contributions from the interdimer Coulomb terms. As shown in Fig. 5(c), there are four configurations of the adjacent dimers A and B, and only the third panel gives V_2 and others zero, which is described by the pseudospin operators as $V_2[1 + \sigma^z_A\sigma^z_B\ (1 - \sigma^z_A)/2]/2$. As $(\sigma^z_A)^2 = 1$ and $\langle\sum_{i=1}^{N}\sigma^z_i\rangle = 0$, this term is reduced to $V_2\sigma^z_A\sigma^z_B/4$ and we find $J' = V_2/4$. The relation $J = (V_3 - V_4)/4$ is constructed in the same manner using V_3 and V_4.

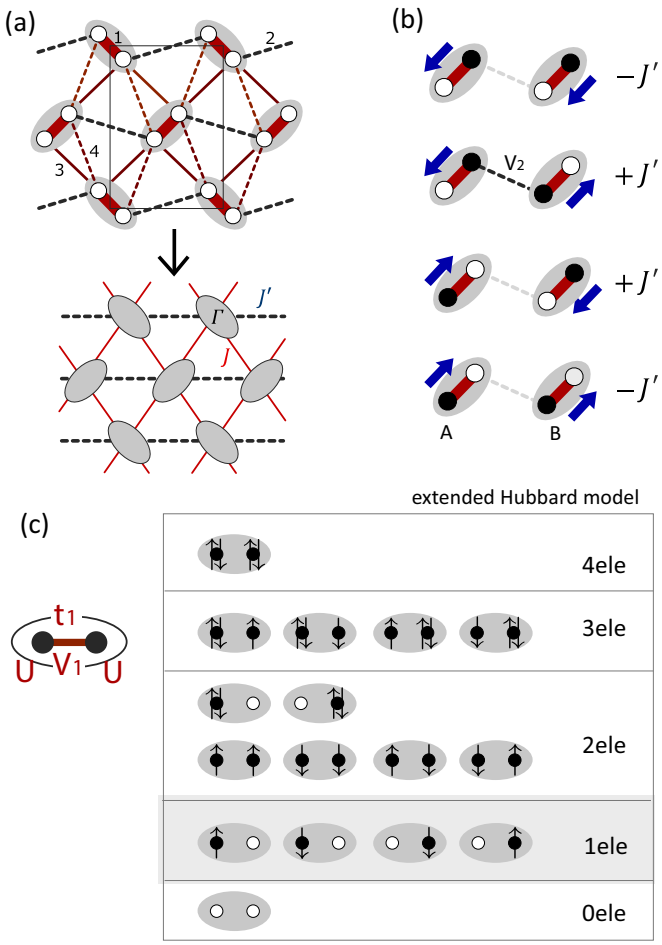

FIG. 5. Schematic description of the models of κ-ET$_2X$. (a) Mapping of the extended Hubbard model based on molecules (circles) to the TRI model based on dimers (ovals). The indices on four independent bonds are those of t_i, V_i, $i = 1 \sim 4$. (b) The 16 basis of the extended Hubbard model on a single dimer, where $\uparrow$ and $\downarrow$ indicate the electrons of up and down spins, respectively. The four different configurations with one electron per dimer form the low-energy local Hilbert space at large V_1, U. When the spin degrees of freedom are neglected at the leading order of perturbation, they are reduced to 2. (c) Configuration of electrons on adjacent two dimers, where the arrows indicate the corresponding pseudospin configuration. The second panel has energy V_2 and others zero, which yields the Ising interactions between pseudospins, see text.

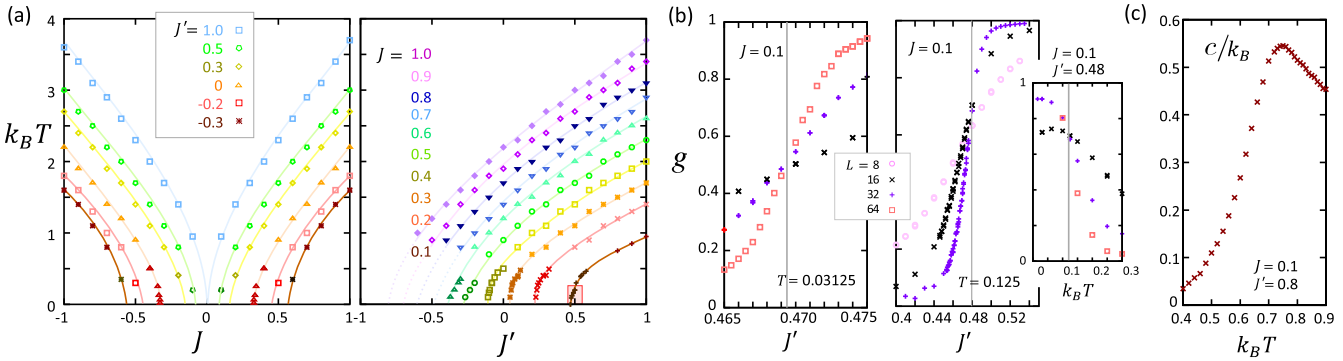

FIG. 6. (a) Phase diagram of the transverse Ising model in Eq. (1) at $\Gamma = 1$ on the triangular lattice. The cross sections of the $J - J' - k_BT$ diagram [small square corresponds to the parameter region of Fig. 2(b) right panel] for several fixed J' on the plane of J and k_BT and for fixed $J = 0.1$–1.0 on the plane of J' and k_BT are shown in two panels. The data points that mark the transition T_c are determined by the crossing of the Binder ratio g for $k_BT \lesssim 0.5$ (deep colored symbols) and as the peak position of the specific heat of $L = 16$ results at $k_BT \gtrsim 0.8$ (light colored symbols). (b) Binder parameter calculated for $L = 8, 16, 32, 64$ at $J = 0.1$ as a function of J' around the phase transition point $J'_c \sim 0.47$ at two low temperatures. The right inset shows the Binder crossing as a function of k_BT that almost coincides with the crossing point of the middle panel, $T_c = 0.125$, $J' \sim 0.4796$. (c) Specific heat c/k_B of $J' = 0.8$, $J = 0.1$ with $L = 16$.

The TRI model Eq. (A2) is the natural low-energy effective model of Eq. (A1) and preserves the symmetry of the original electronic model. Since σ_i^z corresponds to the electric dipole, the "total magnetization" ($\sum_i \sigma_i^z$) is not the true total magnetization of the electronic system but the total electric polarization, which can take any value within the range allowed. We also notice that the dimers A and B are equivalent both in Eq. (A2) and Eq. (A1), although the dimers align in different directions and the crystal inversion symmetry between A and B is slightly broken in real materials.

Substituting the first-principles values of V's to the above relation yields $J/\Gamma \sim 0.1$ and $J'/\Gamma \sim 0.5$ for $\Gamma \sim 200$ meV, and $X = Cu_2(CN)_3$ has slightly larger values than $Cu[N(CN)_2]Cl$. Importantly, it locates in the very vicinity of the QCP ($J/\Gamma = 0.1, J'/\Gamma = 0.47$) in the phase diagram we obtained in Fig. 2(b). We briefly note that Ref. [42] performed a higher-order perturbation with extra terms included compared to Ref. [11].

APPENDIX B: DETAILS OF THE PHASE DIAGRAMS

We present the details of how we obtained the phase diagram given in Fig. 2(b). The cross sections of the phase diagram for fixed J' and J are shown in the two panels of Fig. 6(a). The phase boundaries of $J < 0$ and $J > 0$ are symmetric, and only the positive J part is presented in Fig. 2(b). The square marks the critical region where we intensively studied in the main text. Since we need to precisely evaluate the phase boundaries at low temperatures, we calculated the dimensionless Binder ratio,

$$g = \frac{1}{2}\left(3 - \frac{\langle m^4 \rangle}{\langle m^2 \rangle}\right), \tag{B1}$$

where m is the magnetization density. As shown in Fig. 6(b), their crossing point is almost independent of L and gives a good evaluation of the transition points at low temperatures. The data points at $k_BT \lesssim 0.5$ in Fig. 6(a) are obtained using this analysis.

The overall phase boundaries at $k_BT \gtrsim 0.8$ are evaluated as the peak position of the specific heat density, $c/k_B = (\langle e^2 \rangle - \langle e \rangle^2)N/(k_BT)^2 - \langle n_k \rangle$, in the quantum Monte Carlo simulation, where the last term gives the expectation value of kink density [see Fig. 2(a)] responsible for the quantum fluctuation, required in addition to the fluctuation of energy density e. The data in Fig. 6(c) shows the representative data for $J' = 0.8$, $J = 0.1$ which gives $T_c \sim 0.75$ in the right panel (a).

APPENDIX C: SQUARE LATTICE TRANSVERSE ISING MODEL

We study some other parameters in the phase diagram in Fig. 2(b), i.e., the square lattice ferromagnetic TRI model at $J' = 0$. Qualitatively the same results are obtained for the square lattice. Figures 7(a) and 7(b) are the k_BT dependences of $\chi_{0;L}$ and τ_L to be compared with Fig. 2(d). Here we show both the case at QCP and just off QCP, which follow the exponents of the 3D and 2D Ising universality classes, respectively. The plots of τ and χ_0 on the plane of J and k_BT are shown for a wider temperature range than Fig. 4 in the main text. Although the contour lines are rather different, the overall tendency does not depend on the parameters J and J'. Also, τ and χ_0 extracted from the envelope function of Figs. 7(a) and 7(b) at QCP of the square lattice almost coincide with those of the anisotropic triangular lattice, including the constant coefficients.

We note that the temperature dependences of τ and χ_0 at $J' > J'_c$, namely, when $T_c > 0$, are different from those of the quantum critical point discussed in Eq. (9) in the main text. They follow

$$\tau \propto (T - T_c)^{-z\nu}, \quad \chi_0 \propto (T - T_c)^{-\gamma} \tag{C1}$$

with $z \sim 2.18$, $\nu = 1$, and $\gamma = 1.75$ (see the main text), which belong to the 2D Ising universality class. When fixing the temperature and approaching the phase boundary by varying

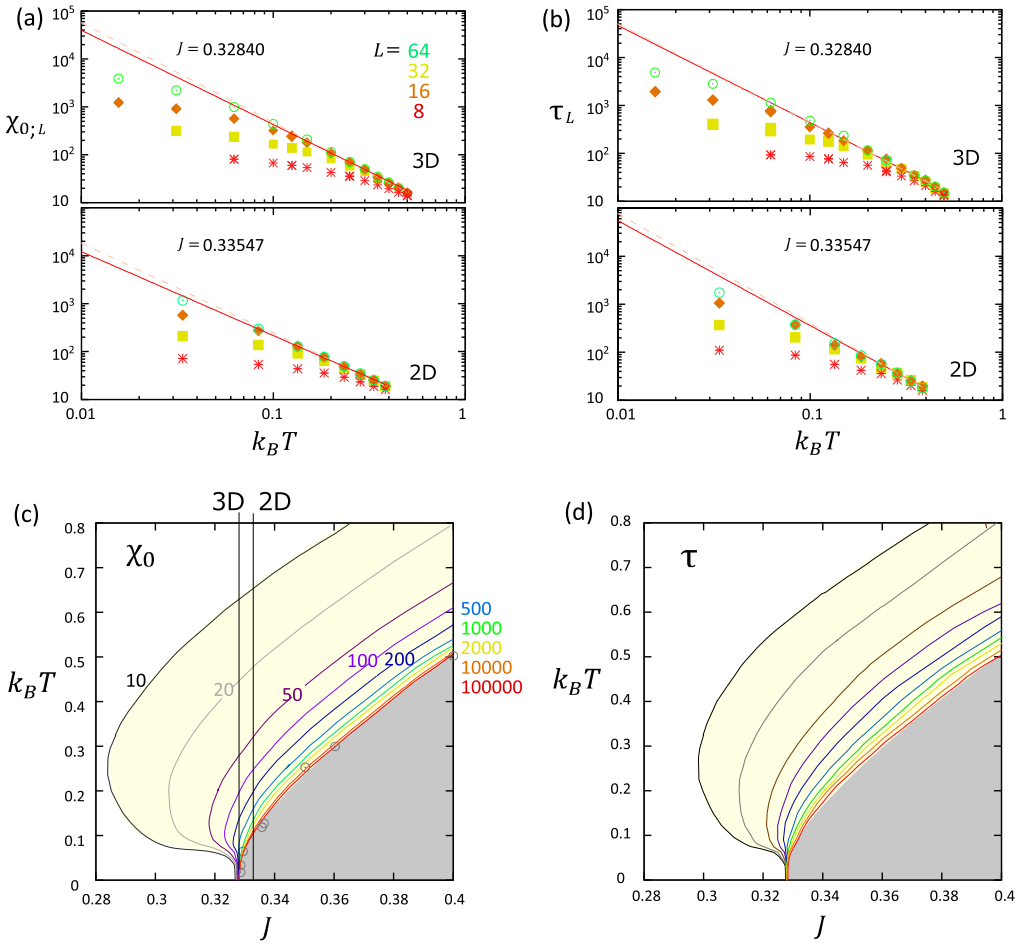

FIG. 7. Results of QMC calculations for the square lattice, $J' = 0$. (a) Static susceptibility $\chi_{0;L}$ and (b) relaxation time τ_L extracted from the relaxation function $\Psi(q = 0, t)$ at $L = 8, 16, 32, 64$, plotted as functions of k_BT for $J = 0.32840$ and 0.33547 at QCP and slightly off QCP. Error bars are smaller than the symbols. The solid and broken lines follow $\tau = c_1(k_BT)^{-z}$ and $\chi_0 = c_2(k_BT)^{-\gamma/\nu}$. The red solid lines follow the critical exponent $(z, \nu, \gamma) = (2.02, 0.629, 1.2379)$ and (2.183,1,1.75) for $J' = 0.32840$ (top) and 0.33547 (bottom) of the 3D and 2D Ising universality class, respectively, where the former (top panel) yields $c_1 = 4.225$, $c_2 = 4.623$, which is similar to the case of the anisotropic triangular lattice [Fig. 2(d)]. Broken lines are the fitted envelope functions describing the thermodynamic limit with an exponent of $(z, \gamma/\nu) = (2.04, 1.87)$ and (2.11,1.74) in the top and bottom panels, respectively. (c, d) Density map of the static susceptibility χ_0 and the relaxation time τ obtained from the Monte Carlo calculation at $J' = 0$ (square lattice), the latter from the kinetic TRI protocol.

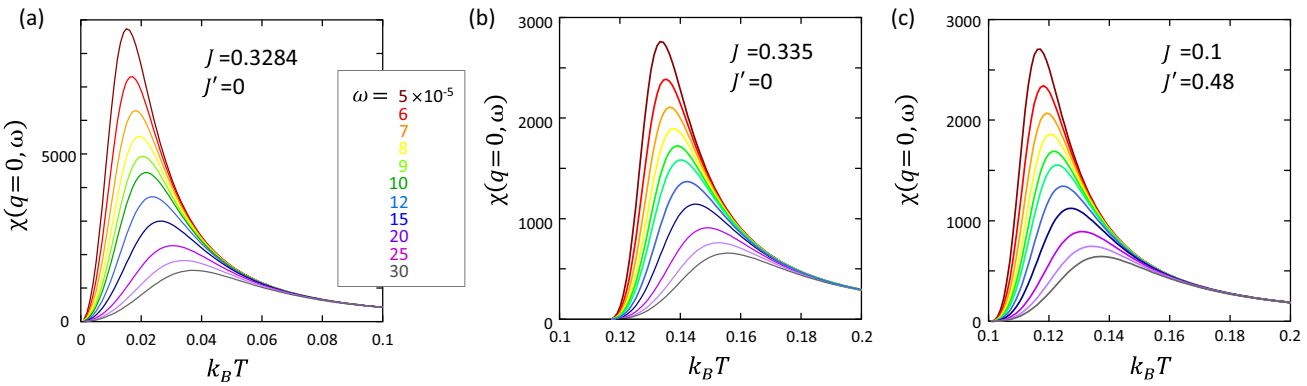

FIG. 8. Dynamic susceptibility, $\chi(q, \omega)$, as a function of k_BT for three different choices of J an J' with $\Gamma = 1$. (a) Square lattice at QCP, $J = 0.3284$, $J' = 0$; (b) square lattice off QCP, $J = 0.3354$, $J' = 0$, with $k_BT_c = 0.1206$; and (c) triangular lattice at QCP, $J = 0.1$, $J' = 0.48$, with $k_BT_c = 0.1163$. Panels (b) and (c) follow the 2D Ising universality class.

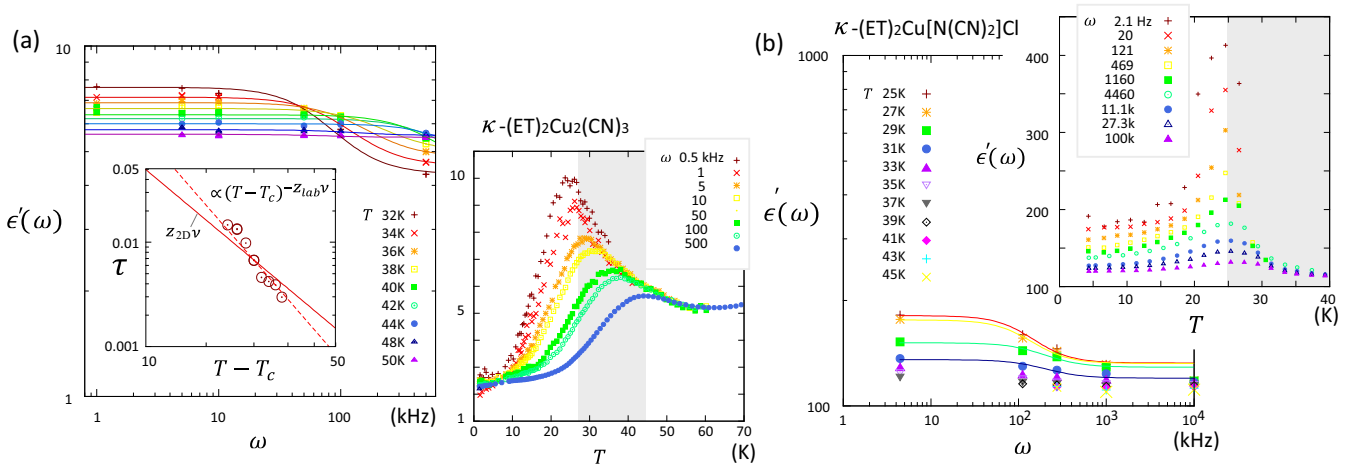

FIG. 9. Dielectric constant $\epsilon'(\omega)$ in units of ϵ_0 of (a) κ-$ET_2Cu_2(CN)_3$ and (b) κ-$ET_2Cu[N(CN)_2]Cl$, reported in Refs. [5,6]. Data is provided by the courtesy of Sasaki and Lunkenheimer. Solid lines are the Lorentzian fit [Eq. (10)], and the value of $\tau_{\rm lab}$ for (a) is given in the inset as functions of $(T - T_c)$ with $T_c = 6$ K. The solid/broken lines in the inset show the function $(T - T_c)^{-z\nu}$ with $z = 2.18$ (2D Ising universality) and 3, respectively.

the model parameters, $g = J$ or J', they follow

$$\tau \propto |g - g_c|^{-z\nu}, \quad \chi_0 \propto |g - g_c|^{-\gamma} \tag{C2}$$

where $g_c = J_c$ or J'_c are the phase boundaries.

APPENDIX D: DYNAMICAL SUSCEPTIBILITY OFF QCP

We here show in Figs. 8(b) and 8(c) the dynamical susceptibility $\chi(q, \omega)$ as a function of k_BT when the model parameter is slightly off QCP. The one at QCP for the square lattice is given together in Fig. 8(a), which is almost the same as that of Fig. 3(c) in the main text. In the case off QCP, χ_0 and τ diverge toward $T_c > 0$, and below T_c, enter the ferro-ordered phase. A similar behavior as that of the QCP is observed, but their critical exponents are that of the 2D universality class, which we confirmed in the calculation in Fig. 7.

APPENDIX E: REEXAMINATION OF THE EXPERIMENTAL RESULTS BY ABDEL-JAWAD *et al.* AND LUNKENHEIMER *et al.*

Based on our theoretical findings, we here reexamine the previous reports on the dielectric measurements of κ-$ET_2Cu_2(CN)_3$ by Abdel-Jawad *et al.* and κ-$ET_2Cu[N(CN)_2]Cl$ by Lunkenheimer *et al.* In these measurements, the dielectric constants in units of ϵ_0 show a peak at temperature $T_m(\omega)$ which distributes at 20–50 K in the former and 25–30 K in the latter material, when the frequency varies from the order of 1 Hz to 100 kHz (see the insets of Fig. 9). These results shall be qualitatively compared to our $\chi(q = 0, \omega)$ besides the constant and the possible experimental background values of ϵ's from a different origin. Let us fix the value of T and extract the experimental data from these figures, and by plotting them against ω we find Figs. 9(a) and 9(b). In the case of κ-$ET_2Cu_2(CN)_3$, the successive crossing of lines belonging to different T takes place over the frequency range of 10–500 kHz to be compared with Fig. 3(b), which can be the origin of the large frequency dependence of T_m. These lines are a Lorentzian fit following Eq. (10) in the main text, and the obtained $\tau_{\rm lab}$ [inset of Fig. 9(a), in units of $(\text{kHz})^{-1}$] varies by one order of magnitude during the temperature change of 10 K. We plot $\tau_{\rm lab}$ against $(T - T_c)$ with $T_c = 6$ K and draw a line proportional to $(T - T_c)^{-z_{\rm lab}\nu}$ with $\nu = 1$. While we cannot precisely determine the exponents as we are not able to extract reliable error bars in fitting ϵ with relatively small numbers of data points, the data seems to fall between $z_{\rm lab} \sim 2.18$ (2D critical exponent, solid line)–3 (broken line). By contrast, in the case of κ-$ET_2Cu[N(CN)_2]Cl$, such crossing does not take place, and τ stays extremely small, of order 10^{-6} $(\text{Hz})^{-1}$ with no significant variation against T.

We thus consider that κ-$ET_2Cu_2(CN)_3$ is in the critical region of the phase diagram, and the frequency dependence is overall understood as a signature of the dynamical criticality. The interpretation of κ-$ET_2Cu[N(CN)_2]Cl$, is not straightforward. The almost frequency-independent behavior indicates that the system is in the disordered phase slightly away from the critical region, whereas τ is very large. One way to reconcile these two tendencies is to notice that κ-$ET_2Cu[N(CN)_2]Cl$ has a Néel order at 27 K, which may be related to the dielectric ordering. If the system is near but off the critical point, the coupling of dipoles with spin degrees of freedom may work as a perturbation to drive the system to the first-order transition of dipoles and magnetism. These couplings indeed emerge in the model one of the authors discussed previously [11,42]. In fact, κ-$ET_2Cu_2(CN)_3$ does not show magnetic ordering down to lowest temperature, which supports this scenario. The first-principles calculation shows that $\Gamma = t_1$ is slightly larger, namely, J/Γ is smaller, for κ-$ET_2Cu[N(CN)_2]Cl$ than κ-$ET_2Cu_2(CN)_3$. This is also consistent with the fact that the former is away from the critical point.

[1] J. Cardy, *Scaling and Renormalization in Statistical Physics* (Cambridge University Press, Cambridge, England, 1996).

[2] S. Sachdev, *Quantum Phase Transitions* (Cambridge University Press, Cambridge, England, 1999).

[3] Y. Kono, T. Sakakibara, C. P. Aoyama, C. Hotta, M. M. Turnbull, C. P. Landee, and Y. Takano, Field-Induced Quantum Criticality and Universal Temperature Dependence of the Magnetization of a Spin-1/2 Heisenberg Chain, Phys. Rev. Lett. **114**, 037202 (2015).

[4] R. Kubo, Statistical-mechanical theory of irreversible processes. I. General theory and simple applications to magnetic and conduction problems, J. Phys. Soc. Jpn. **12**, 570 (1957).

[5] M. Abdel-Jawad, I. Terasaki, T. Sasaki, N. Yoneyama, N. Kobayashi, Y. Uesu, and C. Hotta, Anomalous dielectric response in the dimer Mott insulator κ-(BEDT-TTF)$_2$Cu$_2$(CN)$_3$, Phys. Rev. B **82**, 125119 (2010).

[6] P. Lunkenheimer, J. Muller, S. Krohns, F. Schrettle, A. Loidl, B. Hartmann, R. Rommel, M. de Souza, C. Hotta, J. A. Schlueter, and M. Lang, Multiferroicity in an organic charge-transfer salt that is suggestive of electric-dipole-driven magnetism. Nat. Mater. **11**, 755 (2012).

[7] K. Kanoda, Metal-insulator transition in κ-(ET)$_2X$ and (DCNQI)$_2M$: Two contrasting manifestation of electron correlations, J. Phys. Soc. Jpn. **75**, 051007 (2006).

[8] Y. Shimizu, K. Miyagawa, K. Kanoda, M. Maesato, and G. Saito, Spin Liquid State in an Organic Mott Insulator with a Triangular Lattice, Phys. Rev. Lett. **91**, 107001 (2003).

[9] B. E. Vugmeister and H. A. Rabitz, Phenomenology of relaxor ferroelectrics, Ferroelectrics **201**, 33 (1997).

[10] D. Fu, H. Taniguchi, M. Itoh, and S. Mori, Pb($Mg_{1/3}Nb_{2/3}$)O_3 (PMN) relaxor: Dipole glass or nano-domain ferroelectric? in *Advances in Ferroelectrics* (Intech Open, London, UK, 2012).

[11] C. Hotta, Quantum electric dipoles in spin-liquid dimer Mott insulator κ-$ET_2Cu_2(CN)_3$, Phys. Rev. B **82**, 241104(R) (2010).

[12] M. Naka and S. Ishihara, Electronic ferroelectricity in a dimer Mott insulator, J. Phys. Soc. Jpn. **79**, 063707 (2010).

[13] T. Kadowaki and H. Nishimori, Quantum annealing in the transverse Ising model, Phys. Rev. E **58**, 5355 (1998).

[14] J. Brooke, D. Bitko, T. F. Rosenbaum, and G. Aeppli, Quantum annealing of a disordered magnet, Science **284**, 779 (1999).

[15] H. Fukuyama, J. Kishine, and M. Ogata, Energy landscape of charge excitations in the boundary region between Dimer-Mott and charge ordered states in molecular solids, J. Phys. Soc. Jpn. **86**, 123706 (2017).

[16] T. Koretsune and C. Hotta, Evaluating model parameters of the κ- and β'-type Mott insulating organic solids, Phys. Rev. B **89**, 045102 (2014).

[17] K. Nakamura, Y. Yoshimoto, T. Kosugi, R. Arita, and M. Imada, Ab initio derivation of low-energy model for κ-ET type organic conductors, J. Phys. Soc. Jpn. **78**, 083710 (2009).

[18] H. O. Jeschke, M. de Souza, R. Valentí, R. S. Manna, M. Lang, and J. A. Schlueter, Temperature dependence of structural and electronic properties of the spin-liquid candidate κ-(BEDT-TTF)$_2$Cu$_2$(CN)$_3$, Phys. Rev. B **85**, 035125 (2012).

[19] S. R. White and A. E. Feiguin, Real-Time Evolution Using the Density Matrix Renormalization Group, Phys. Rev. Lett. **93**, 076401 (2004).

[20] G. Vidal, Efficient Simulation of One-Dimensional Quantum Many-Body Systems, Phys. Rev. Lett. **93**, 040502 (2004).

[21] H. Endo, C. Hotta, and A. Shimizu, From Linear to Nonlinear Responses of Thermal Pure Quantum States, Phys. Rev. Lett. **121**, 220601 (2018).

[22] O. F. Syljuåsen, Using the average spectrum method to extract dynamics from quantum Monte Carlo simulations, Phys. Rev. B **78**, 174429 (2008).

[23] C. De Grandi, A. Polkovnikov, and A. W. Sandvik, Universal nonequilibrium quantum dynamics in imaginary time, Phys. Rev. B **84**, 224303 (2011).

[24] C.-W. Liu, A. Polkovnikov, and A. W. Sandvik, Quasi-adiabatic quantum Monte Carlo algorithm for quantum evolution in imaginary time, Phys. Rev. B **87**, 174302 (2013).

[25] R. J. Glauber, Time-dependent statistics of the Ising model, J. Math. Phys. **4**, 294 (1963).

[26] T. Nakamura and Y. Ito, A quantum Monte Carlo algorithm realizing an intrinsic relaxations, J. Phys. Soc. Jpn. **72**, 2408 (2003).

[27] R. Martoňák, G. E. Santoro, and E. Tosatti, Quantum annealing by the path-integral Monte Carlo method: The two-dimensional random Ising model, Phys. Rev. B **66**, 094203 (2002).

[28] T. Ikegami, S. Miyashita, and H. Rieger, Quantum versus classical annealing of Ising spin glasses, Science **348**, 215 (2015).

[29] S. Yin, C.-Y. Lo, and P. Chen, Scaling behavior of quantum critical relaxation dynamics of a system in a heat bath, Phys. Rev. B **93**, 184301 (2016).

[30] B. Blaß and H. Rieger, Test of quantum thermalization in the two-dimensional transverse-field Ising model, Sci. Rep. **6**, 38185 (2016).

[31] J. Schachenmayer, A. Pikovski, and A. M. Rey, Many-Body Quantum Spin Dynamics with Monte Carlo Trajectories on a Discrete Phase Space, Phys. Rev. X **5**, 011022 (2015).

[32] T. Ikegami, S. Miyashita, and H. Rieger, Griffiths-McCoy singularities in the transverse field Ising model on the randomly diluted square lattice, J. Phys. Soc. Jpn. **67**, 2671 (1998).

[33] M. Collura, Off-equilibrium relaxational dynamics with an improved Ising Hamiltonian, J. Stat. Mech. (2010) P12036.

[34] S. Wansleben and D. P. Landau, Dynamical critical exponent of the 3D Ising model, J. Appl. Phys. **61**, 3968 (1987).

[35] F. Gliozzi and A. Rago, Critical exponents of the 3d Ising and related models from conformal bootstrap, J. High Energy Phys. 10 (2014) 042.

[36] M. Hasenbusch, Finite size scaling study of lattice models in the three-dimensional Ising universality class, Phys. Rev. B **82**, 174433 (2010).

[37] N. Ito, Non-equilibrium relaxation and interface energy of the Ising model, Physica A **196**, 591 (1993).

[38] N. Ito, Simulation of time exponent in 2D Glauber kinetic Ising model, Physica A **184**, 201 (1992).

[39] B. Dammann and J. D. R. Reger, Dynamical critical exponent of the two-dimensional Ising model, Europhys. Lett. **21**, 157 (1993).

[40] M. Abdel-Jawad, N. Tajima, R. Kato, and I. Terasaki, Disordered conduction in single-crystalline dimer Mott compounds, Phys. Rev. B **88**, 075139 (2013).

[41] J. Müller, S. Iguchi, H. Taniguchi, and T. Sasaki, Formation of nanoscale polarized clusters as precursors of electronic ferroelectricity probed by conductance noise spectroscopy, Phys. Rev. B **102**, 100103(R) (2020).

[42] M. B. Deglint, K. Akella, and M. P. Kennett, Charge glass in an extended dimer Hubbard model, Phys. Rev. B **106**, 085123 (2022).

[43] K. Mitsumoto, C. Hotta, and H. Yoshino, Spin-Orbital Glass Transition in a Model of a Frustrated Pyrochlore Magnet without Quenched Disorder, Phys. Rev. Lett. **124**, 087201 (2020).

[44] M. J. P. Gingras, C. V. Stager, N. P. Raju, B. D. Gaulin, and J. E. Greedan, Static Critical Behavior of the Spin-Freezing Transition in the Geometrically Frustrated Pyrochlore Antiferromagnet $Y_2Mo_2O_7$, Phys. Rev. Lett. **78**, 947 (1997).

[45] C. Hotta, K. Ueda, and M. Imada, Quantum mechanically driven structural-spin glass in two dimensions at finite temperature, arXiv:2207.07293.

[46] D. Khomskii, Classifying multiferroics: Mechanisms and effects, Physics **2**, 20 (2009).

[47] M. Pinterić, M. Čulo, O. Milat, M. Basletić, B. Korin-Hamzić, E. Tafra, A. Hamzić, T. Ivek, T. Peterseim, K. Miyagawa, K. Kanoda, J. A. Schlueter, M. Dressel, and S. Tomić, Anisotropic charge dynamics in the quantum spin-liquid candidate κ-(BEDT-TTF)$_2$Cu$_2$(CN)$_3$, Phys. Rev. B **90**, 195139 (2014).

[48] K. Sedlmeier, S. Elsässer, D. Neubauer, R. Beyer, D. Wu, T. Ivek, S. Tomić, J. A. Schlueter, and M. Dressel, Absence of charge order in the dimerized κ-phase BEDT-TTF salts, Phys. Rev. B **86**, 245103 (2012).

[49] M. Lang, P. Lunkenheimer, J. Muller, A. Loidl, B. Hartmann, N. H. Hoang, E. Gati, H. Schubert, and J. A. Schlueter, Multiferroicity in the Mott insulating charge-transfer salt κ-(BEDT-TTF)$_2$Cu[N(CN)$_2$]Cl, IEEE Trans. Magn. **50**, 2700107 (2014).

[50] S. Iguchi, S. Sasaki, N. Yoneyama, H. Taniguchi, T. Nishizaki, and T. Sasaki, Relaxor ferroelectricity induced by electron correlations in a molecular dimer Mott insulator, Phys. Rev. B **87**, 075107 (2013).

[51] K. Itoh, H. Itoh, M. Naka, S. Saito, I. Hosako, N. Yoneyama, S. Ishihara, T. Sasaki, and S. Iwai, Collective Excitation of an Electric Dipole on a Molecular Dimer in an Organic Dimer-Mott Insulator, Phys. Rev. Lett. **110**, 106401 (2013).

[52] Y. Hattori, S. Iguchi, T. Sasaki, S. Iwai, H. Taniguchi, and H. Kishida, Electric-field-induced intradimer charge disproportionation in the dimer-Mott insulator β'-(BEDT-TTF)$_2$ICl$_2$, Phys. Rev. B **95**, 085149 (2017).

[53] F. Nad, P. Monceau, C. Carcel, and J. M. Fabre, Dielectric response of the charge-induced correlated state in the quasi-one-dimensional conductor (TMTTF)$_2$PF$_6$, Phys. Rev. B **62**, 1753 (2000).

[54] P. Monceau, F. Y. Nad, and S. Brazovskii, Ferroelectric Mott-Hubbard Phase of Organic (TMTTF)$_2X$ Conductors, Phys. Rev. Lett. **86**, 4080 (2001).

[55] S. P. Shen, J. C. Wu, J.-D. Song, X. F. Sun, Y. F. Yang, Y. S. Chai, D.-S. Shang, S.-G. Wang, J. F. Scott, and S. Young, Quantum electric-dipole liquid on a triangular lattice, Nat. Commun. **7**, 10569 (2016).

[56] S. E. Rowley, L. J. Spalek, R. P. Smith, M. P. M. Dean, M. Itoh, J. F. Scott, G. G. Lonzarich, and S. S. Saxena, Ferroelectric quantum criticality, Nat. Phys. **10**, 367 (2014).

[57] H. Seo, C. Hotta, and H. Fukuyama, Toward systematic understanding of diversity of electronic properties in low-dimensional molecular solids, Chem. Rev. **104**, 5005 (2004).